Volume 1 | Number 1 | Jan 2013 | Pages 1–100

# Nanoscale

www.rsc.org/nanoscale

ROYAL SOCIETY OF CHEMISTRY

ROYAL SOCIETY OF CHEMISTRY

www.rsc.org/nanoscale

# Constructing Fe₂O₃/TiO₂ Core-Shell Photoelectrodes for Efficient Photoelectrochemical Water Splitting

SCHOLARONE™
Manuscripts

**ARTICLE TYPE**

# Constructing Fe₂O₃/TiO₂ Core-Shell Photoelectrodes for Efficient Photoelectrochemical Water Splitting

**Meng Wang,** [a, b] **Myeongwhun Pyeon,** [b] **Yakup Gönüllü,** [b] **Ali Kaouk,** [b] **Shaohua Shen,** [a] **Liejin Guo,** [a*] **and Sanjay Mathur** [a,b*]

In this study, plasma enhanced chemical vapor deposition (PECVD) was utilized to co-axially modify hydrothermally grown Fe₂O₃ nanorod arrays by depositing TiO₂ overlayer to create Fe₂O₃/TiO₂ core-shell photoelectrodes. Comprehensive structural (XRD, SEM; TEM) and compositional (XPS) analyses were
10 performed to understand the effects of TiO₂ shell on the PEC activities of Fe₂O₃ core. It was revealed that the heterojunction structure, formed between TiO₂ and Fe₂O₃, significantly improved the separation efficiency of photo-induced charge carriers and the oxygen evolution kinetics. A maximum photocurrent density of ~ 900 $\mu$A/cm$^2$ at 0.6 V *vs.* saturated calomel electrode (SCE) was obtained for Fe₂O₃/TiO₂ photoelectrodes, which was 5 and 18 times higher when compared to that of hydrothermally synthesized
15 Fe₂O₃ and PECVD synthesized TiO₂ electrodes, respectively. Moreover, the Fe₂O₃/TiO₂ core-shell nanorod arrays displayed superior stability for PEC water splitting. During 5000 sec PEC measurements, a steady decrease of the photocurrent was observed mainly attributed to the evolution of oxygen bubbles adsorbed on the working electrodes. This observation was verified by the complete recovery of the PEC performance demonstrated for second 5000 sec PEC measurement carried out after a brief time interval
20 (10 min) that allowed the electrode surface to regenerate.

## 1. Introduction

The growing realization that fossil resources will run out in this century and the green-house effect caused by the combustion of hydrocarbon fuels is adversely affecting the global climate has
25 significantly triggered the research interests in exploiting recyclable, earth-abundant and environmental friendly resources for energy production [1-2]. Ever since the discovery of PEC water splitting effect by applying TiO₂ thin film as photoanodes and Pt plate as the counter-electrode [3], research has significantly
30 progressed in converting solar energy to chemical fuels such as solar-hydrogen. A huge amount of solar energy ( 3*10²⁴ Joules) reaches the earth surface every year, which is 10,000 times higher than the current global consumption [1]. Hydrogen is believed to be an ideal energy carrier because of achievable high energy density,
35 storability, and clean combustion leaving water as the only by-product. However, the traditional strategies for producing hydrogen (such as water electrolysis or hydrocarbon reformation) suffer severely from high costs and environmental pollution [4].

For efficient solar hydrogen production, photoactive
40 semiconductor catalysts are of critical importance as they should unify various materials characteristics in a single system [5-7]. Besides a relatively narrow-band gap (1.8-2.5 eV), required to harvest most of the visible light region of solar spectrum; excellent separation efficiency for photogenerated electron and
45 hole pairs and long-term stability in water splitting reaction

conditions are the major prerequisites that make the identification of a champion material a synthetic challenge [8-12]. Among numerous materials such as metal oxides, sulfides, nitrides, phosphides and other compositions investigated for PEC water
50 splitting [13-19], transition metal oxides have attracted much interest due to their intrinsically high chemical stability and high abundance. Metal sulfides and metal nitrides usually contain a much smaller band gap, but their poor stabilities significantly limited their further application for PEC applications [20-11]. On the
55 other hand, metal oxides usually exhibit a wide-band gap (> 3.0 eV) that makes them poor photo-absorbers in visible range and indicate the necessity of band gap adjustment by electronic doping or structural modifications such as core-shell or multi-layered morphology that allow harvesting maximum incident
60 photons.

Fe₂O₃ exhibits excellent visible light absorption ability and is considered to be an ideal candidate for PEC water splitting. With a band gap of 1.9-2.2 eV, the theoretical solar-to-chemical energy conversion efficiency for Fe₂O₃ was calculated to be 16% [22-23]. In
65 addition to its promising optical absorption ability, Fe₂O₃ also displayed superior stability and is non-toxic. As a result, numerous efforts have been made for Fe₂O₃ based PEC applications [23], however, the obtained PEC water splitting efficiencies so far were still lower than the theoretical value
70 largely due to low concentration of photo-generated charge carriers, short hole diffusion length and sluggish oxygen evolution kinetics that suppressed the PEC water splitting

efficiency of $Fe_2O_3$ [24-25].

Given the properties of half-filled d-orbitals, $Fe_2O_3$ with $d^5$ electron configuration exhibits less charge carriers and lower mobility than corresponding transition metal oxides with unfilled or mostly-filled d orbits [23]. Therefore, numerous efforts have been made to dope the iron oxide lattice with various cations such as Zn, Ti, Sn, Zr and Ta in order to increase the amount of charge carriers and their mobility [27-30]. The literature reports suggest that cation doping is an efficient means to regulate the lattice parameters, improve the charge carrier concentration and their separation efficiency, and ultimately the PEC water splitting ability. Surface modification of photoelectrode is shown to be another promising approach for improved PEC ability. For example, decorating $Fe_2O_3$ surface with a water oxidation co-catalyst such as Co-Pi [31-32] can significantly improve its oxygen evolution kinetics. Also, deposition of a passivation layer was found to improve the PEC performance of $Fe_2O_3$ by passivating its surface recombination centers [33].

In this study, hydrothermally synthesized $Fe_2O_3$ nanorod arrays were successfully modified with a $TiO_2$ overlayer deposited by PECVD technique. $Fe_2O_3/TiO_2$ composites with core-shell nanostructures behave as cooperative photo-systems that resemble the tandem band energy structure occurring in natural photosynthesis [34]. Promoted by external driving force created by the applied potential at the interface between $Fe_2O_3/TiO_2$ heterojunctions, the transfer of photogenerated electron and hole pairs can be effectively improved. As a result, improved PEC performance was obtained for $Fe_2O_3/TiO_2$ core-shell nanorod arrays. In addition, $Fe_2O_3/TiO_2$ core-shell nanorod arrays prepared in this study showed superior PEC stability, displaying almost unchanged photocurrent density during 5000 sec measurement cycles.

## 2. Experimental

### 2.1 Fabrication of β-FeOOH nanorod arrays

A facile hydrothermal method was utilized to synthesis iron oxyhydroxide (β-FeOOH) nanorods as described by Vayssieres [35], but with a minor modification. Typically, 0.15 M of ferric chloride ($FeCl_3$, 0.73 g) and 1 M of sodium nitrate ($NaNO_3$, 2.55 g) were dissolved into 30 ml deionized water with continuous magnetic stirring, and then the pH value of the solution was set at 1.5 with hydrochloride (HCl). After 15 min magnetic stirring, the solution was transferred into a steel-lined Teflon autoclave with a cleaned fluorine-doped tin oxide substrate (FTO from Sigma Aldrich) placed against the wall of the Teflon tube. The autoclave was then maintained at 120 °C for 24 h. Finally, the β-FeOOH nanorod arrays could be obtained after washing with deionized water and ethanol for several times, and after a post-annealing treatment, pure $Fe_2O_3$ nanorod arrays could be obtained.

### 2.2 Fabrication of $Fe_2O_3/TiO_2$ core-shell nanorod arrays

Plasma-assisted chemical vapor deposition of titanium isopropoxide ($Ti(OPr^i)_4$) was utilized to introduce a $TiO_2$ shell on as-prepared β-FeOOH nanorod arrays. Typically, β-FeOOH nanorod arrays coated FTO substrates were firstly placed in the chamber of the PECVD machine (Plasma Electronic, Neuenburg, Germany). Then, a round bottom glass flask containing a certain amount of titanium precursor was connected to the reaction system. The glass flask was maintained at 70 °C to make sure the precursor was at a sufficient vapor pressure. After the chamber was pumped down to a pressure lower than 0.5 Pa, 20 sccm $O_2$ were introduced into the chamber. After PECVD approach with plasma power of 100 W for different time, coated β-FeOOH nanorod arrays with different $TiO_2$ thickness were obtained. $Fe_2O_3/TiO_2$ core-shell nanorod arrays could be obtained after the post annealing treatment at 750 °C for 2 h. For pure $TiO_2$ film deposition, FTO glass without β-FeOOH nanorods was utilized as the substrate for PECVD approach.

### 2.3 Morphological and structural characterization

The X-ray diffraction (XRD) patterns were obtained from a STOE-STADI MP diffractometer operating in the reflection mode using Cu Kα (λ = 1.5406 Å) radiation. The chemical composition was obtained by X-ray photoelectron spectroscopy (XPS) on ESCA M-Probe (Al Kα) with an energy resolution of 0.8 eV. The charge calibration was performed by correcting C1s peak of adventitious carbon setting to 284.8 eV to compensate the charge effect. The sample morphology was observed by a Zeiss NEON 40 scanning electron microscope (SEM) and Zeiss LEO 912 transmission electron microscope (TEM). Raman spectra were obtained by a triple grating micro-Raman spectrometer (T64000, Jobin Yvon).

### 2.4 Photoelectrochemical measurements of the photoanodes

A three-electrode system was utilized for the PEC measurements, in which $Fe_2O_3/TiO_2$ core-shell nanorod arrays mounted onto a home-designed electrode holder served as the working electrode, a saturated calomel electrode (SCE) served as reference electrode, and a platinum wire with a large exposed area served as the counter electrode. The surface area exposed to the electrolyte was fixed at 0.785 cm$^2$, and 1 M aqueous solution of sodium hydroxide was utilized as the electrolyte. Amperometric photocurrent-potential (I-V) and photocurrent-time (I-t) measurement were obtained by a SMU (source/monitor unit) E 5272A with two Medium Power SMU modules E5282A by Agilent. The light source was a 75 W Xe-lamp (model 71208, Newport and a Solar Simulator SSR buLuzchem) with an AM 1.5 G filter.

## 3. Results and discussion

A two-step method was utilized to synthesis $Fe_2O_3/TiO_2$ core-shell nanorod arrays. In the first step, β-FeOOH nanorod arrays were synthesized by a facile hydrothermal method, and later converted to one-dimensional $Fe_2O_3$ structures (Fig. 1a) after a post-annealing treatment (Temperature 750 °C). $Fe_2O_3$ nanorods with the diameters ranging from 30 nm to 70 nm were grown on the FTO substrate, which demonstrated quite smooth surfaces and homogeneous coverage (inset, in Fig. 1(a)). In the second step, PECVD was performed to deposit $TiO_2$ layer on $Fe_2O_3$ nanorods. After 10 min $TiO_2$ deposition, $TiO_2$ particles were observed on the surfaces of $Fe_2O_3$ nanorods (Fig. 1(b) and inset in Fig. 1(b)). When the deposition time was increased to 30 min, $Fe_2O_3/TiO_2$ core-shell nanorods with complete coverage of the iron oxide cores was observed that produced nanostructrues of diameters larger than 200 nm. Longer deposition time resulted in thicker $TiO_2$ coatings that filled the intergranular voids among nanorods

and thus led to decreased contact area with the electrolyte (Fig. 1(d)), which ultimately suppressed the PEC water splitting ability [36-37].
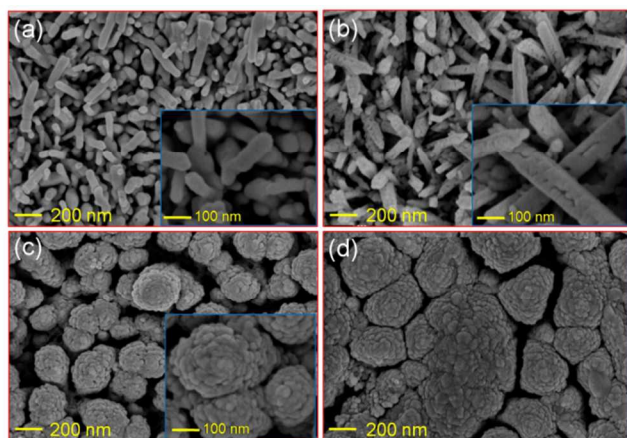


Fig. 1 SEM images of pristine $Fe_2O_3$ (a) and $Fe_2O_3/TiO_2$ core-shell nanorod arrays with different PECVD treating-time for $TiO_2$ deposition (b-10 min, c-30 min d-60 min).

Cross-sectional SEM images of pristine $Fe_2O_3$ and $Fe_2O_3/TiO_2$ nanostructures exhibited $Fe_2O_3$ nanorods in the diameters ranging from 30-70 nm randomly grown on FTO substrate (Fig. 2a), while the length of pristine $Fe_2O_3$ nanorods was about 600 nm. $TiO_2$ deposition performed for short time-periods (10 min) produced, small $TiO_2$ nanoparticles that uniformly covered $Fe_2O_3$ nanorods, leading to enlarged diameter and thickness (~ 720 nm), as shown in Fig. 2(b). When the PECVD treatment time was extended to 60 min, $Fe_2O_3/TiO_2$ core-shell nanorod arrays with much larger diameters and thickness (~ 1200 nm) were obtained (Fig. 2c and d). More interestingly, $Fe_2O_3/TiO_2$ core-shell columnar arrays demonstrated tapered top surfaces possibly due to the template effects, hydrothermally grown $Fe_2O_3$ nanorods also had a tapered morphology, as illustrated in Fig. 3 [38-41].
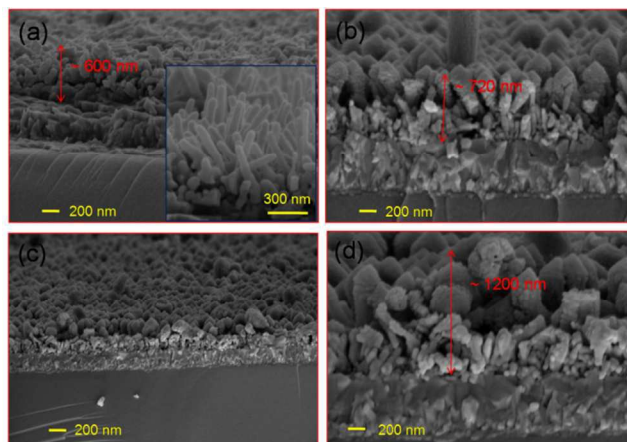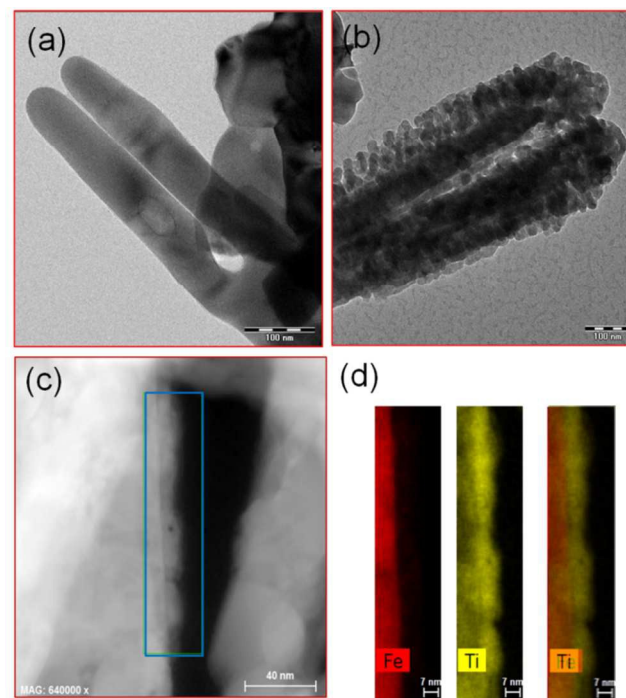


Fig. 2 Cross-sectional SEM images of pristine $Fe_2O_3$ (a) and $Fe_2O_3/TiO_2$ core-shell nanorod arrays (b, 10 min deposition for $TiO_2$ deposition, c and d, 60 min deposition for $TiO_2$).

In order to confirm the core-shell nanostructure of the composite films of $Fe_2O_3$ and $TiO_2$, TEM measurements and elemental mapping (Fig. 4 and Fig. S1) were performed in this study. Whereas pristine $Fe_2O_3$ nanorods displayed a single crystalline structure, a strongly rough surface composed of small $TiO_2$ particles resulted upon the PECVD treatment. The surface enhancement as well as defined interface between the core and shell compositions are evident in Fig. 4(b). Fig. 4(d) shows the elemental EDX mapping results of the selected area in Fig. 4(c), displaying the spatially distribution of Fe and Ti elements. It is revealed that Fe element was only located in the core region of the nanorod and Ti element can be observed not only in the core region but also in the shell region, suggesting uniform core-shell structure of $Fe_2O_3$ and $TiO_2$. Moreover, the overlapped image of Fe and Ti elemental mapping images (the third image in Fig. 4(d)) matched very well with the selected area in Fig. 4(c). Large area elemental mapping measurements were also conducted as illustrated in Fig. S1 in the Electronic Supplementary Information, suggesting a homogenous lateral distribution of $TiO_2$ species over $Fe_2O_3$ nanorods.
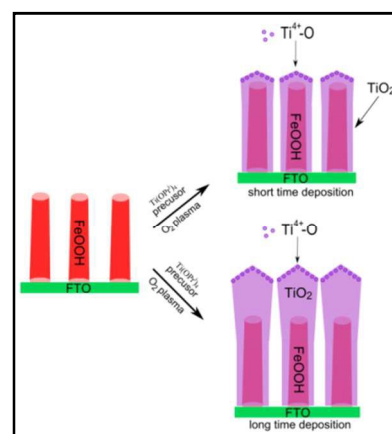


Fig. 3 Schematic diagram of the growth mechanism for $Fe_2O_3/TiO_2$ core-shell nanorod arrays with short time or long time deposition.



Fig. 4 TEM images of pristine $Fe_2O_3$ (a), $Fe_2O_3/TiO_2$ core-shell nanorod arrays with 20 min deposition for $TiO_2$ layer (b and c), and TEM mapping images of selected area in (c).

Fig. 5 shows XRD patterns of pristine $Fe_2O_3$ and $TiO_2$ decorated $Fe_2O_3$ nanorod arrays. For pristine $Fe_2O_3$, diffraction peaks arose at 2θ=35.74 ° and 54.58 ° (marked with "α") could be assigned to (110) and (116) planes of rhombohedral $Fe_2O_3$
[5] (reference code: 00-073-1764). All other peaks at 26.28 °, 33.77 °, 37.77 °, 51.76 °, 61.75 °, and 65.74 ° (marked with "∗") were attributed to (110), (101), (200), (211), (310), and (301) planes, respectively of tetragonal $SnO_2$ (reference code: 00-046-1088). The origin of these diffraction peaks was the FTO substrate,
[10] composed of fluoride doped $SnO_2$. After $TiO_2$ deposition, a new peak arose at 25.37 ° corresponding to (101) planes of anatase $TiO_2$ (reference code: 01-073-1764) was observed, which was marked with "δ". Because of the small amount of deposited $TiO_2$, no diffraction peak belonging to TiFe-720 nm was observed. As
[15] the thickness of the film was increased from 900 nm to 1200 nm, $Fe_2O_3/TiO_2$ core-shell nanorod arrays yielded more intensive (101) diffraction peak, in accordance with the larger amount of $TiO_2$ being deposited, which was verified by SEM and TEM analyses. No other peaks were detected in the XRD patterns,
[20] suggesting the films to consist of only $Fe_2O_3$ and $TiO_2$. To further confirm the crystal phase of $Fe_2O_3$ and $TiO_2$, Raman scattering measurements were performed. According to space group symmetry and factor group analysis, $α-Fe_2O_3$ exhibits 7 Raman-active vibration modes $(2A_{1g} + 5E_g)$ [42]. The Raman peaks arose at
[25] 223 $cm^{-1}$, 290 $cm^{-1}$, 409 $cm^{-1}$ and 606 $cm^{-1}$ in Fig. S2, could be assigned to typical $A_{1g}$, $E_g$, $E_g$ and $E_g$ modes of $α-Fe_2O_3$ [43], whereas $γ-Fe_2O_3$ display obviously different Raman peaks, as described in precious literature [44]. Except for Raman peaks of $Fe_2O_3$, $E_g$ (151 $cm^{-1}$), intrinsically weak $E_g$ (196 $cm^{-1}$) and high
[30] frequency $E_g$ (633 $cm^{-1}$) vibration modes of anatase $TiO_2$ were also observed for composite $Fe_2O_3/TiO_2$ samples [45], confirming the $Fe_2O_3/TiO_2$ core-shell nanorod arrays were composed of α phase $Fe_2O_3$ core and anatase phase $TiO_2$ shell.
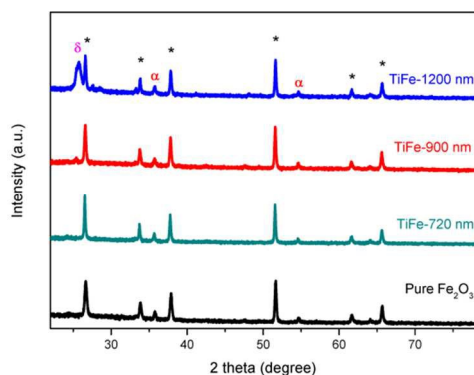


[35] **Fig. 5** XRD patterns of pristine $Fe_2O_3$ and $Fe_2O_3/TiO_2$ core-shell nanorod arrays with TiFe-900 nm refers to the sample with a thickness around 900 nm and TiFe-1200 nm refers to the sample with a thickness around 1200 nm. The different symbols in this graph related to different components with "∗" refers to $SnO_2$, "α" refers to $Fe_2O_3$ and "δ" refers to $TiO_2$.

[40] The chemical composition of $Fe_2O_3/TiO_2$ films was further investigated by XPS technique (Fig. 6). Before $TiO_2$ deposition, XPS peaks of pristine $Fe_2O_3$ corresponded to O 1s, Fe 2p and C 1s suggesting the presentence of Fe and O elements, while the carbon peak originated from the adventitious carbon. The binding
[45] energies of Fe $2p_{1/2}$ and Fe $2p_{3/2}$ were located at *ca.* 710.3 eV and 724.0 eV, confirming as the presence of $Fe^{3+}$ [46-47]. Fig. 6(c) shows the survey-scan XPS spectra of $Fe_2O_3/TiO_2$ with a thickness

around 720 nm. In addition to the chemical binding energies belonging to C 1s, O 1s, Fe 2p, the peaks assignable to Ti 2p and
[50] 2s were also observed. Owing to the core-shell structure, $TiO_2$ deposits significantly decreased the peak intensity of Fe 2p. When the film thickness was further increased to around 900 nm, no binding peaks according to Fe could be observed, which is in accordance with the surface-sensitive nature of XPS technique
[55] (Fig. S3). The high-resolution XPS spectra of Ti 2p in Fig. 6(d) showed that the binding energies of Ti $2p_{3/2}$ and Ti $2p_{1/2}$ were located at 458.2 eV and 463.8 eV, respectively, which matched well with the typical binding energy values of $TiO_2$ [48-49]. Possible formation of $FeTiO_3$ was not observed due to the low processing
[60] temperature [50].
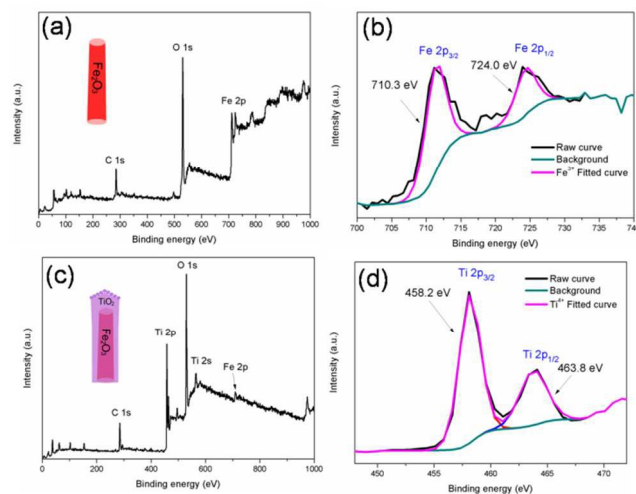


**Fig. 6** Survey-scan XPS spectra (a) and XPS Fe 2p spectra of pristine $Fe_2O_3$; survey-scan XPS spectra (c) and XPS Fe 2p spectra of $Fe_2O_3/TiO_2$ core-shell nanorod arrays with a thickness around 720 nm.

[65] Fig. 7(a) and (b) illustrate the I-V performance of pristine $Fe_2O_3$ and $Fe_2O_3/TiO_2$ core-shell nanorod arrays. All the samples demonstrated negligible photocurrent density in dark, indicating their good stability in the present PEC system. However, upon exposure to simulated solar irradiation, pristine $Fe_2O_3$, $TiO_2$ and
[70] $TiO_2$ decorated $Fe_2O_3$ nanorod arrays displayed different photocurrent densities. For pristine $Fe_2O_3$ and $TiO_2$, steady increase in photocurrent densities was observed, which reached the maximum value of about ~ 175 $μA/cm^2$ and ~ 50 $μA/cm^2$ at 0.6 V *vs.* SCE, respectively. For $TiO_2$ covered $Fe_2O_3$ nanorod
[75] arrays, at lower applied potential, the photocurrent of $Fe_2O_3/TiO_2$ core-shell nanorod arrays increased slowly, whereas when the applied potential reached a certain value, the photocurrent densities demonstrated a rapid increase (Fig. 7(b)). This was due to the type-I heterojunction structure between $Fe_2O_3$ and $TiO_2$, as
[80] shown in Fig. 7(c and d) [51-52]. The conduction band of $TiO_2$ is more negative and its valence band is more positive than those of $Fe_2O_3$. Therefore, at low or without overpotential the holes transfer from $Fe_2O_3$ to $TiO_2$ was suppressed (Fig. 7(c)), which led to decreased PEC performance for the core-shell nanorod arrays.
[85] However, when higher overpotential was applied, more significant band bending in $Fe_2O_3$ could be created, which made photo-induced holes energetic enough to cross the potential barrier between the valence bands of $Fe_2O_3$ and $TiO_2$ (Fig. 7(d)).

Besides, the nanoparticle morphology of $TiO_2$ remarkably increased the contact area between the photoelectrodes and electrolyte, which also played significant roles in determining the PEC performance. Nevertheless, thick $TiO_2$ layer might create
5 more grain boundaries between $TiO_2$ nanoparticles, which, to some extent, restricted the transfer of photogenerated electrons. Along with the advantages of forming core-shell nanostructure between $Fe_2O_3$ and $TiO_2$, Ti doping was also expected because of the solid state diffusion effect during the post-annealing approach.
10 By using different substrates in the preparation of $Fe_2O_3$ nanorod arrays, Grimes et al. [53] demonstrated Ti and Sn diffusion from the substrates to $Fe_2O_3$ nanorod arrays during high temperature annealing approach. Ti and Sn can effectively improve the amount of charge carrier density and their mobility, and therefore
15 much improved PEC performance was obtained for Ti and Sn doped $Fe_2O_3$ nanorod arrays. The composite sample with ~900 nm thickness showed the maximum photocurrent density of ~ 900 $\mu A/cm^2$ at 0.6 V *vs.* SCE, which was comparable with the photocurrent values of $Fe_2O_3/TiO_2$ composite films prepared with
20 different methods described in Table 1.
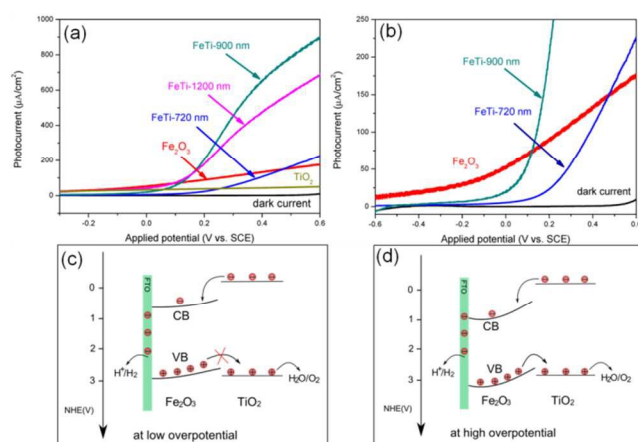


**Fig. 7** I-V curves (a) and partially enlarged I-V curves (b) of pristine $Fe_2O_3$ and $Fe_2O_3/TiO_2$ core-shell nanorod arrays with different thicknesses. Schematic diagram of the band structure and charge transfer
25 of $Fe_2O_3/TiO_2$ heterojunction at low overpotential (c), and high overpotential (d). (Light resource: 75 W Xe lamp with AM 1.5 G filter; Electrolyte: 1 M of NaOH aqueous solution; Counter electrode: Pt; and Reference electrode: SCE).

Time depended (I-t) measurement was also conducted in this
30 study to investigate the stability of the $Fe_2O_3/TiO_2$ nanorod arrays with core-shell structure for PEC water splitting, as shown in Fig. 8. During 5000 sec measurement, the photocurrent increased firstly at the beginning and then decreased slowly. More importantly, this sample demonstrated a higher PEC performance
35 for second measurement. The increase of the photocurrent at beginning could be assigned to the activation effect. After the activation effect, the photocurrent density of $Fe_2O_3/TiO_2$ decreased slowly. This was due to the produced oxygen bubbles on the photoanode surface decreased the contact area between photoelectrode and electrolyte. In order to investigate the long-
40 term stability of the $Fe_2O_3/TiO_2$ photoelectrode, 10 h I-t measurement was applied for the same sample with 900 nm thickness, as shown in Fig. S4. This measurement was carried out with two stages. Four hours measurement was firstly performed,
45 and then the electrolyte was changed for another six hours

measurement. During long-term measurement, the photocurrent density decreased slowly. Two reasons led to this decrease, one is the decay of $Fe_2O_3/TiO_2$ core-shell nanorod arrays and the other is the adsorption of the produced oxygen bubbles on sample
50 surfaces. When the adsorbed oxygen bubbles released from the sample surface, sudden increase of the photocurrent density could be observed (Fig. S4). After 10 h measurement, we took a picture of the working electrode (Fig. S5), which clearly displayed the existence of big oxygen bubbles at the sample surface.
55 Fortunately, several strategies have been developed such as utilizing rotating or specially designed electrodes, which have been described in other literatures [57-58].

Table1. Photocurrent densities of $Fe_2O_3/TiO_2$ composite films prepared with different methods.

| Nr. | Photocurrent (mA/cm$^2$) | Preparation method | References |
|---|---|---|---|
| 1. | 0.3 (at 0.4 V vs. Ag/AgCl with visible light illumination) | $TiO_2$: wet-chemical method, $Fe_2O_3$: wet-chemical method | 54 |
| 2. | 0.2 (at 0.6 V vs. Ag/AgCl) | $TiO_2$: hydrothermal method $Fe_2O_3$: sol-flame method | 47 |
| 3. | 0.46 (at 0.1 V vs. SCE) | $TiO_2$: anodic oxidation $Fe_2O_3$: chemical bath deposition | 51 |
| 4. | 1.65 (at 0.95 V vs. SCE) | $Zn-Fe_2O_3$: spray pyrolysis $Fe-TiO_2$: spray pyrolysis | 55 |
| 5. | 0.683 (at 1.5 V vs. RHE with visible light illumination) | $TiO_2$: spin coating $Fe_2O_3$: two-phase hydrolysis-solvothermal reaction | 56 |
| Result in this study | 0.9 (at 0.6 V vs. SCE) | $TiO_2$: PECVD $Fe_2O_3$: hydrothermal method | |
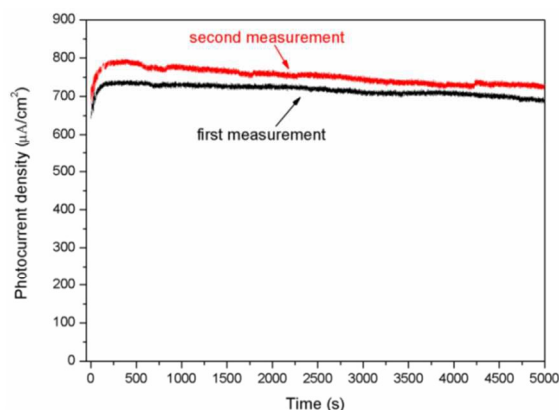


60
**Fig.8** I-t curves of $Fe_2O_3/TiO_2$ core-shell nanorod arrays with a thickness around 900 nm. (Light resource: 75 W Xe lamp with AM 1.5 G filter; Electrolyte: 1 M of NaOH aqueous solution; Counter electrode: Pt; Reference electrode: SCE; and Applied potential: 0.5 V).

65 **4. Conclusion**

In this study, surface modification of hydrothermally synthesized $Fe_2O_3$ nanorod arrays by PECVD-deposited $TiO_2$ overlayers is examined with respect to the PEC properties of single-phase and composite nanostructures. The well-defined phase boundaries and
70 differential band gap energies of the individual metal oxides enables the formation of a tandem heterojunction structure between $Fe_2O_3$ and $TiO_2$ that improves the separation efficiency

of photogenerated electron-hole pairs with higher applied potential. Under the illumination of simulated solar light, the composite film with a thickness around 900 nm displayed maximum photocurrent density of ~ 900 µA/cm$^2$ at 0.6 V *vs.* SCE, which was 5 times and 18 times higher than those of hydrothermally synthesized $Fe_2O_3$ and PECVD synthesized $TiO_2$, respectively. Furthermore, this unique nanostructure also demonstrated superior stability for PEC water splitting during 10 h PEC measurement. This study to prepare 1D photoelectrodes with uniform core-shell structure will provide some insights for developing new kinds of heterojunction based photoanodes for solar energy conversion.

## Acknowledgement

## Notes and references

$^a$ International Research Center for Renewable Energy, State Key Laboratory of Multiphase Flow in Power Engineering, Xi'an Jiaotong University, Shaanxi 710049, China. Email: shshen_xjtu@mail.xjtu.edu.cn; lj-guo@mail.xjtu.edu.cn.
$^b$ Department of Inorganic Chemistry, University of Cologne, Greinstr. 6, 50939 Cologne, Germany. Email: mathurs@uni-koeln.de

† Electronic Supplementary Information (ESI) available: TEM-EDX mapping images, Survey-scan XPS spectra, I-t measurement of $Fe_2O_3/TiO_2$ core-shell nanorod arrays, and Digital photograph of the PEC cell after 10 h I-t measurement are available. See DOI: 10.1039/b000000x/

1. M. Grätzel, *Nature,* 2001, **414**, 338-344.
2. X. Chen, S. Shen, L. Guo and S. S. Mao, *Chemical Reviews,* 2010, **110**, 6503-6570.
3. A. Fujishima and K. Honda, *nature,* 1972, **238**, 37-38.
4. X. Lu, S. Xie, H. Yang, Y. Tong and H. Ji, *Chemical Society reviews,* 2014, **43(22)**, 7581-7593.
5. D. Barreca, G. Carraro, A. Gasparotto, C. Maccato, C. Sada, A. P. Singh, S. Mathur, A. Mettenborger, E. Bontempi and L. E. Depero, *International Journal of Hydrogen Energy,* 2013, **38**, 14189-14199.
6. A. P. Singh, A. Mettenborger, P. Golus and S. Mathur, *International Journal of Hydrogen Energy,* 2012, **37**, 13983-13988.
7. J. T. Li, M. W. G. Hoffmann, H. Shen, C. Fabrega, J. D. Prades, T. Andreu, F. Hernandez-Ramirez and S. Mathur, *J. Mater. Chem,* 2012, **22**, 20472-20476.
8. A. Kudo and Y. Miseki, *Chemical Society Reviews,* 2009, **38**, 253-278.
9. H. Wang, S. Kalytchuk, H. Yang, L. He, C. Hu, W. Y. Teoh and A. L. Rogach, *Nanoscale,* 2014, **6**, 6084-6091.
10. K. Sivula, R. Zboril, F. Formal, R. Robert, A. Weidenkaff, J. Tucek, J. Frydrych and M. Gratzel, *Journal of the American Chemical Society,* 2010, **132**, 7436-7444.
11. A. Paracchino, V. Laporte, K. Sivula, M. Gratzel and E. Thimsen, *Nature Materials,* 2011, **10**, 456-461.
12. S. Emin, F. F. Abdi, M. Fanetti, W. Peng, W. Smith, K. Sivula, B. Dam and M. Valant, *J. Electroanalyt. Chem.* 2014, **717-718**, 1-24.
13. J. Han, F. Fan, C. Xu, S. Lin, M. Wei, X. Duan and Z. L. Wang, *Nanotechnology,* 2010, **21**, 405203.
14. Y. Lai, Z. Lin, D. Zheng, L. Chi, R. Du and C. Lin, *Electrochimica Acta,* 2012, **79**, 175-181.
15. X. Sun, K. Maeda, M. Le Faucheur, K. Teramura and K. Domen, *Applied Catalysis a-General,* 2007, **327**, 114-121.
16. Q. J. Xiang, J. G. Yu and M. Jaroniec, *J. Phys. Chem. C,* 2011, **115**, 7355-7363.
17. S. C. Yan, Z. S. Li and Z. G. Zou, *Langmuir,* 2009, **25**, 10397-10401.
18. J. Pan, S. M. Hühne, H. Shen, L. Xiao, P. Born, W. Mader and S. Mathur, *The Journal of Physical Chemistry C,* 2011, **115**, 17265-17269.
19. S. Emin, M. de Respinis, M. Fanetti, W. Smith, M. Valant and B. Dam, *Applyed Catalysis B: Environment,* 2015, **166-167**, 406-412.
20. R. M. N. Yerga, M. C. A. Galvan, F. del Valle, J. A. V. de la Mano and J. L. G. Fierro, *ChemSusChem,* 2009, **2**, 471-485.
21. K. Maeda, T. Takata, M. Hara, N. Saito, Y. Inoue, H. Kobayashi and K. Domen, *Journal of the American Chemical Society,* 2005, **127**, 8286-8287.
22. S. Shen, *Journal of Materials Research,* 2014, **29**, 29-46.
23. C. Kronawitter, I. Zegkinoglou, S. H. Shen, P. Liao, I. Cho, O. Zandi, Y. S. Liu, K. Lashgari, G. Westin and J. H. Guo, *Energy & Environmental Science,* 2014, **7**, 3100-3121.
24. A. Kay, I. Cesar and M. Grätzel, *Journal of the American Chemical Society,* 2006, **128**, 15714-15721.
25. S. Shen, C. X. Kronawitter, J. Jiang, S. S. Mao and L. Guo, *Nano Research,* 2012, **5**, 327-336.
26. V. R. Satsangi, *Current Science,* 2006, **91**, 8.
27. Y. S. Hu, A. Kleiman-Shwarsctein, G. D. Stucky and E. W. McFarland, *Chem. Commun,* 2009, **19**, 2652-2654.
28. N. T. Hahn and C. B. Mullins, *Chemistry of Materials,* 2010, **22**, 6474-6482.
29. P. Kumar, P. Sharma, R. Shrivastav, S. Dass and V. R. Satsangi, *International Journal of Hydrogen Energy,* 2011, **36**, 2777-2784.
30. M. R. Gholipour, T. C. Dinh, F. Béland and T. O. Do, *Nanoscale,* 2015.
31. M. Barroso, A. J. Cowan, S. R. Pendlebury, M. Grätzel and D. R. Klug, J. R. Durrant, *Journal of the American Chemical Society,* 2011, **133**, 14868-14871.
32. D. K. Zhong, M. Cornuz, K. Sivula, M. Grätzel and D. R. Gamelin, *Energy & Environmental Science,* 2011, **4**, 1759-1764.
33. R. Franking, L. S. Li, M. A. Lukowski, F. Meng, Y. Z. Tan, R. J. Hamers and S. Jin, *Energy & Environmental Science,* 2013, **6**, 500-512.
34. R. Hill and F. A. Y. Bendall, *Nature,* 1960, **186**, 136-137.
35. L. Vayssieres, N. Beermann, S. E. Lindquist and A. Hagfeldt, *Chemistry of materials,* 2001, **13**, 233-235.
36. N. N. Zhao, C. C. He, J. B. Liu, H. J. Gong, T. An, H. X. Xu, F. Q. Zhao, R. Z. Hu, H. X. Ma and J. Z. Zhang, *J. Solid State Chem.,* 2014, **219**, 67-73.
37. S. W. Zhang, J. X. Li, H. H. Niu, W. Q. Xu, J. Z. Xu, W. P. Hu and X. K. Wang, *ChemPlusChem,* 2013, **78**, 192-199.
38. A. Borras, A. Barranco and A. González-Elipe, *Journal of Materials Science,* 2006, **41**, 5220-5226.
39. S. Mathur and P. Kuhn, *Surface and Coatings Technology,* 2006, **201**, 807-814.
40. S. Mathur, M. Veith, V. Sivakov, H. Shen, V. Huch, U. Hartmann and H. B. Gao, *Chem. Vapor Depos.,* 2002, **8**, 277-283.
41. A. Mettenbörger, T, Singh, A. P. Singh, T. T. Järvi, M. Moseler, M. Valldor and S. Mathur, *International Journal of Hydrogen Energy,* 2014, **39**, 4828-4835.
42. A. Zoppi, C. Lofrumento, E. M. Castellucci and P. Sciau, *Journal of Raman Spectroscopy,* 2008, **39**, 40-46.
43. C. Baratto, P. Lottici, D. Bersani, G. Antonioli, G. Gnappi and A. Montenero, *Journal of sol-gel science and technology,* 1998, **13**, 667-671.
44. C. Pascal, J. Pascal, F. Favier, M. Elidrissi Moubtassim and C. Payen, *Chemistry of materials,* 1999, **11**, 141-147.
45. W. Zhang, Y. He, M. Zhang, Z. Yin and Q. Chen, *Journal of Physics D: Applied Physics,* 2000, **33**, 912.
46. M. A. Mahadik, S. S. Shinde, V. S. Mohite, S. S. Kumbhar, A. V. Moholkar, K. Y. Rajpure, V. Ganesan, J. Nayak, S. R. Barman and C.

H. Bhosale, *Journal of Photochemistry and Photobiology. B, Biology,* 2014, **133**, 90-98.

47.  N. Sobti, A. Bensouici, F. Coloma, C. Untiedt and S. Achour, *Journal of Nanoparticle Research,* 2014, **16**, 1-10.

5 48.  H. Zhu, J. Tao and X. Dong, *The Journal of Physical Chemistry C,* 2010, 114, 2873-2879.

49.  G. Liu, W. Jaegermann, J. He, V. Sundström and L. Sun, *The Journal of Physical Chemistry B,* 2002, **106**, 5814-5819.

50.  A. Raghavender, N. H. Hong, K. J. Lee, M. H. Jung, Z. Skoko, M. 
10  Vasilevskiy, M. Cerqueira and A. Samantilleke, *Journal of Magnetism and Magnetic Materials,* 2013, **331,** 129-132.

51.  S. Kuang, L. Yang, S. Luo and Q. Cai, *Applied Surface Science,* 2009, **255**, 7385-7388.

52.  W. H. Hung, T. M. Chien and C. M. Tseng, *The Journal of Physical* 
15  *Chemistry C,* 2014, 12676-12681.

53.  D. D. Qin, C. L. Tao, S. i. In, Z. Y. Yang, T. E. Mallouk, N. Bao and C. A. Grimes, *Energy & Fuels,* 2011, **25,** 5257-5263.

54.  P. Luan, M. Xie, D. Liu, X. Fu and L. Jing, *Scientific Reports,* 2014, **4**, 6180.

20 55.  P. Sharma, P. Kumar, A. Solanki, R. Shrivastav, S. Dass and V. R. Satsangi, *Journal of Solid State Electrochemistry,* 2011, **16**, 1305-1312.

56.  C. Zhang, Q. Wu, X. Ke, J. Wang, X. Jin and S. Xue, *International Journal of Hydrogen Energy,* 2014, **39**, 14604-14612.

25 57.  Y. Liang, Y. Li, H. Wang, J. Zhou, J. Wang, T. Regier and H. Dai, *Nature materials,* 2011, **10**, 780-786.

58.  M. Gong, Y. Li, H. Wang, Y. Liang, J. Z. Wu, J. Zhou, J. Wang, T. Regier, F. Wei and H. Dai, *J Am Chem Soc,* 2013, **135**, 8452-8455.

30